APPLIED SCIENCES AND ENGINEERING

Simultaneous electromechanical monitoring in engineered heart tissues using a mesoscale framework

Dominic E. Fullenkamp[1]†, Woo-Youl Maeng[2,3]†, Seyong Oh[4]†, Haiwen Luan[2,3,5], Kyung Su Kim[2,3,6,7], Ivana A. Chychula[1], Jin-Tae Kim[2,3,8], Jae-Young Yoo[9], Cory W. Holgren[1], Alexis R. Demonbreun[1], Sharon George[10,11], Binjie Li[10], Yaching Hsu[2,3,10], Gooyoon Chung[12], Jeongmin Yoo[12], Jahyun Koo[6,7], Yoonseok Park[12,13]*, Igor R. Efimov[10,14]*, Elizabeth M. McNally[1]*, John A. Rogers[2,3,10,15,16]*

Engineered heart tissues (EHTs) generated from human induced pluripotent stem cell–derived cardiomyocytes (hiPSC-CMs) represent powerful platforms for human cardiac research, especially in drug testing and disease modeling. Here, we report a flexible, three-dimensional electronic framework that enables real-time, spatiotemporal analysis of electrophysiologic and mechanical signals in EHTs under physiological loading conditions for dynamic, noninvasive, longer-term assessments. These electromechanically monitored EHTs support multisite measurements throughout the tissue under baseline conditions and in response to stimuli. Demonstrations include uses in tracking physiological responses to pharmacologically active agents and in capturing electrophysiological characteristics of reentrant arrhythmias. This platform facilitates precise analysis of signal location and conduction velocity in human cardiomyocyte tissues, as the basis for a broad range of advanced cardiovascular studies.

INTRODUCTION

Human induced pluripotent stem cell–derived cardiomyocytes (hiPSC-CMs) have changed the landscape of cardiovascular research by providing access to a reliable source of human cardiomyocytes that can be reproducibly differentiated from hiPSCs by well-established, reproducible protocols (1, 2). Small-animal models of cardiovascular disease often fall short in recapitulating key aspects of human cardiac disease, partly mediated by considerable differences in heart rate, heart size, and protein isoform expression (3). For example, in the mouse α-myosin heavy chain is the predominant myosin heavy chain isoform in the ventricle, whereas β-myosin heavy chain in humans, is the predominant human ventricular isoform (4, 5). In addition, the high heart rate of small-animal models reflects physiologically critical differences in ion channel expression and Ca^{2+} handling. Larger-animal models can improve phenotyping but are impractical, cost-prohibitive, and unable to replicate many aspects of human myocardial disorders (6). Given the limitations of animal models in predicting the safety and efficacy of human response to drugs, the FDA Reauthorization Act 2.0 now allows for animal-free alternatives in developing new drugs (7, 8). hiPSC-CMs are well positioned to serve as a valuable model for both mechanistic and translational cardiovascular science including drug development, especially as they have a human genomic context (9). Successful translation requires, however, improved physiological readouts from hiPSC-CMs.

Most hiPSC-CM work has been conducted in a two-dimensional (2D) cell culture monolayer format. These models suffer from non-physiologic culture conditions, immaturity, and a limited capacity to measure clinically relevant outputs such as contractility and arrhythmia propensity (9–11). Engineered heart tissues (EHTs) are created by embedding hiPSC-CMs with (12) or without fibroblasts or other cells (13) into a hydrogel matrix or decellularized tissue scaffolds (14). Such EHTs promote improved cardiomyocyte alignment and maturity. These systems allow for the application of load using flexible support posts, which is not possible using typical rigid 2D culture platforms (15). In this way, physiologic outputs such as contractile force and contraction velocity can be directly measured (12, 13). EHTs promote hiPSC-CM maturation with improved sarcomere alignment and protein localization and, by some reports, nascent T-tubule formation (15). While approaches for the dynamic monitoring of contractile force have been developed (16, 17), continuous, nonterminal integration with electrophysiologic monitoring remains a key challenge. Arrhythmia modeling in EHTs has largely been limited to terminal experiments using membrane voltage–sensitive dyes requiring toxic myosin inhibition with agents like blebbistatin (18). Multi-electrode arrays (MEAs) can support continuous field potential and impedance measurements, but such technologies are limited to the 2D cell culture format (19).

[1]Center for Genetic Medicine, Bluhm Cardiovascular Institute, Northwestern University Feinberg School of Medicine, Chicago, IL 60611, USA. [2]Querrey Simpson Institute for Bioelectronics, Northwestern University, Evanston, IL 60208, USA. [3]Center for Bio-Integrated Electronics, Northwestern University, Evanston, IL 60208, USA. [4]Division of Electrical Engineering, Hanyang University ERICA, Ansan 15588, Republic of Korea. [5]Department of Mechanical and Aerospace Engineering, University of California, San Diego, La Jolla, CA 92093, USA. [6]School of Biomedical Engineering, Korea University, Seoul 02841, Republic of Korea. [7]Interdisciplinary Program in Precision Public Health, Korea University, Seoul 02841, Republic of Korea. [8]Department of Mechanical Engineering, Pohang University of Science and Technology, Pohang 37673, Republic of Korea. [9]Department of Semiconductor Convergence Engineering, Sungkyunkwan University, Suwon 16417, Republic of Korea. [10]Department of Biomedical Engineering, Northwestern University, Evanston, IL 60208, USA. [11]Department of Pharmacology and Chemical Biology, University of Pittsburgh, Pittsburgh, PA 15260, USA. [12]Department of Advanced Materials Engineering for Information and Electronics, Integrated Education Institute for Frontier Science & Technology (BK21 Four), Kyung Hee University, Yongin 17104, Republic of Korea. [13]KHU-KIST Department of Converging Science and Technology, Kyung Hee University, Seoul 02447, Republic of Korea. [14]Department of Medicine, Northwestern University, Chicago, IL 60611, USA. [15]Department of Materials Science and Engineering, Northwestern University, Evanston, IL 60208, USA. [16]Department of Neurological Surgery, Northwestern University, Chicago, IL 60611, USA.
*Corresponding author. Email: yoonseok.park@khu.ac.kr (Y.P.); igor.efimov@northwestern.edu (I.R.E.); elizabeth.mcnally@northwestern.edu (E.M.M.); jrogers@northwestern.edu (J.A.R.)
†These authors contributed equally to this work.

Micropatterning, pacing, and application of mechanical stress can enhance the translational potential of 2D culture hiPSC-CMs (*20*), and advanced monitoring of spherical cardiac organoid formats has been reported (*21*). However, the resulting outputs are limited due to the aforementioned shortcomings of 2D culture methods and the lack of cellular alignment in spherical organoids relative to the 3D EHT format. Adaptation of conventional electronics for electrophysiologic interrogation, electrical stimulation, and mechanical monitoring has been hampered by the mechanical mismatch between rigid conventional sensors and soft, mechanically active tissues.

Through advances in materials science and engineering, soft and flexible electronics can now be created with a variety of sensing capabilities, including force, strain, temperature, pH, and electrical potential (*22*, *23*) in both 2D and 3D architectures. In particular, beyond conventional 2D MEAs, which are limited to the bottom contact area of 3D organoids, geometries across the entire 3D surface offer great potential for organoid recording. For example, a shell-shaped MEA based on a bilayer, self-folding polymer for brain organoids provides a larger recording contact area compared to conventional MEAs (*24*). Another example involves a 3D MEA formed using a mechanical assembly process similar to the one used here, designed to gently wrap the entire spheroid surface with a collection of thin, flexible electronic and optoelectronic elements (*23*). In addition, self-rolling biosensor arrays have been used to support multiplexed monitoring with high sensitivity and spatiotemporal resolution for cardiac organoids (*25*). In addition, these platforms allow for electrical stimulation, which has clinical therapeutic relevance in pacemakers and defibrillators (*26*). This report leverages previously reported 3D systems, referred to as 3D multifunctional mesoscale frameworks (3D-MMFs), to create a 3D electromechanically monitored EHT platform that integrates electrodes and strain sensors distributed onto constructs mechanically tuned to support auxotonic EHT contraction. A range of experiments demonstrates reproducible, noninvasive, spatiotemporally monitoring during which field potential and contraction dynamics are correlated in EHTs over a period of weeks. The direct integration of flexible electronics with EHTs enables nonterminal electrophysiology (EP) studies in these tissues using stimulation techniques similar to those used on human hearts in the clinical EP laboratory. Here, we demonstrate an ability to provoke and sustain reentrant rhythms, highlighting the potential utility of this platform to model clinically relevant cardiac tachyarrhythmias.

RESULT
EHTs integrated with flexible 3D-MMFs
The device introduced here allows for real-time electrophysiologic sensing, pacing, and contractility assessments of EHTs under physiologic loading conditions. Figure 1A depicts the integration of a ~5.1-mm ring-shaped EHT onto a flexible 3D-MMF consisting of a multipost structure that includes six electrodes and six strain sensors distributed in a circular array, with defined physiologic auxotonic loading conditions. This system enables simultaneous acquisition of electrophysiological and mechanical behaviors at multiple, well-defined locations along circular-shaped EHTs, in real time. This 3D-MMF follows from geometrical transformation of a symmetrical 2D precursor with a custom design guided by finite element analysis (fig. S1), using adapted versions of concepts reported elsewhere (fig. S2) (*23*, *27*, *28*). Thin, mechanically compliant arc-shaped

features define posts that include pairs of extended features and tissue supports to stabilize the mounted cardiac ring during culture. These structures ensure optimal, repeatable positioning of the ring with stable contact to each post and electrode (Fig. 1B) for measurements of local field potentials (Fig. 1C, left). Strain sensors, also integrated with each post, respond to bending induced by tissue contraction (Fig. 1C, right). The electrodes have dimensions of 0.82×0.22 mm and consist of electroplated nanocluster platinum (0.5 to 1.0 µm) as a uniform (fig. S4) and low-impedance interface [~4 kilohm at 1 kHz in a phosphate-buffered saline (PBS) solution (fig. S5)] for high-quality electrophysiological recordings (Fig. 1D, top). The overall framework relies on a multilayer of polyimide (PI; 5 µm)/Cr/Au (10/200 nm)/PI (5 µm) (fig. S3).

Mechanical loading is a normal part of myocardial physiology and, in excess, it drives pathophysiology, as in hypertensive cardiomyopathy or, in animal models, transverse aortic constriction to induce a pressure-overloaded state (*29*). Longitudinal tissue loading and force generation depends on the tissue and loading geometry. The posts have a low bending stiffness ($k = 1.32$ µN/µm; fig. S8) such that, using the geometric constraints particular to our platform and others, the loading conditions for this 3D-MMF (4.63×10^{-5} mN·mm/cell) are comparable to those of a standard commercial system (3.75×10^{-5} mN·mm/cell; 2-post, Myriamed; details of calculations are in Materials and Methods) and similar to those reported by others (*30*). Modified engineering designs can deterministically address a range of loading conditions relevant to study requirements.

The lower part of Fig. 1D shows a serpentine trace (width of 3 µm; initial resistance, 1.4 to 1.7 kilohm) as a strain gauge that exhibits a linear change in resistance with applied force [formula, $15.7x - 0.04$ (fig. S8)]. This gauge integrates into a Wheatstone bridge with two identical fixed resistors. The output of this circuit, driven by a regulated dropout voltage (5 V), passes through an instrument amplifier (INA322, Texas Instruments) with a gain of 1000 (v/v) to yield a voltage difference (ΔV) between the initial voltage and those induced by deformation of the framework. The signal then passes through a low-pass filter (fig. S6), to allow comprehensive real-time characterization of tissue contraction and relaxation dynamics under defined systolic (Fig. 1F) and diastolic (Fig. 1G) loading conditions.

EHTs form by embedding 750,000 cells in a collagen-based hydrogel matrix using 90% hiPSC-CMs differentiated through a standard ventricular differentiation protocol (*2*, *31*) and 10% human cardiac fibroblasts (*30*). Tissues are initially matured in ring-shaped polydimethylsiloxane (PDMS) molds, followed by 7 days of remodeling (fig. S8) and then are manually mounted onto the 3D-MMF. These ring-shaped tissues have inner and outer diameters of ~4.4 and ~5.1 mm, respectively. The shape-matched 3D-MMF provides a mechanism for gentle tissue contact with the recording electrodes, secured with two tissue supports on each post of 3D-MMF (Fig. 1, B and E). Figure 1H shows a representative demonstration of time-synchronized field potential (red line) from one electrode and the signal (blue line) from the strain sensor on the same post. These synchronized data allow precise correlation of electrical and mechanical responses during different phases of the cardiac cycle.

Simultaneous spatiotemporal monitoring
The platform allows real-time electrophysiologic and contractility assessment under physiologic loading conditions. The time-synchronized electrical measurement system includes an amplifier (INTAN 128 ch
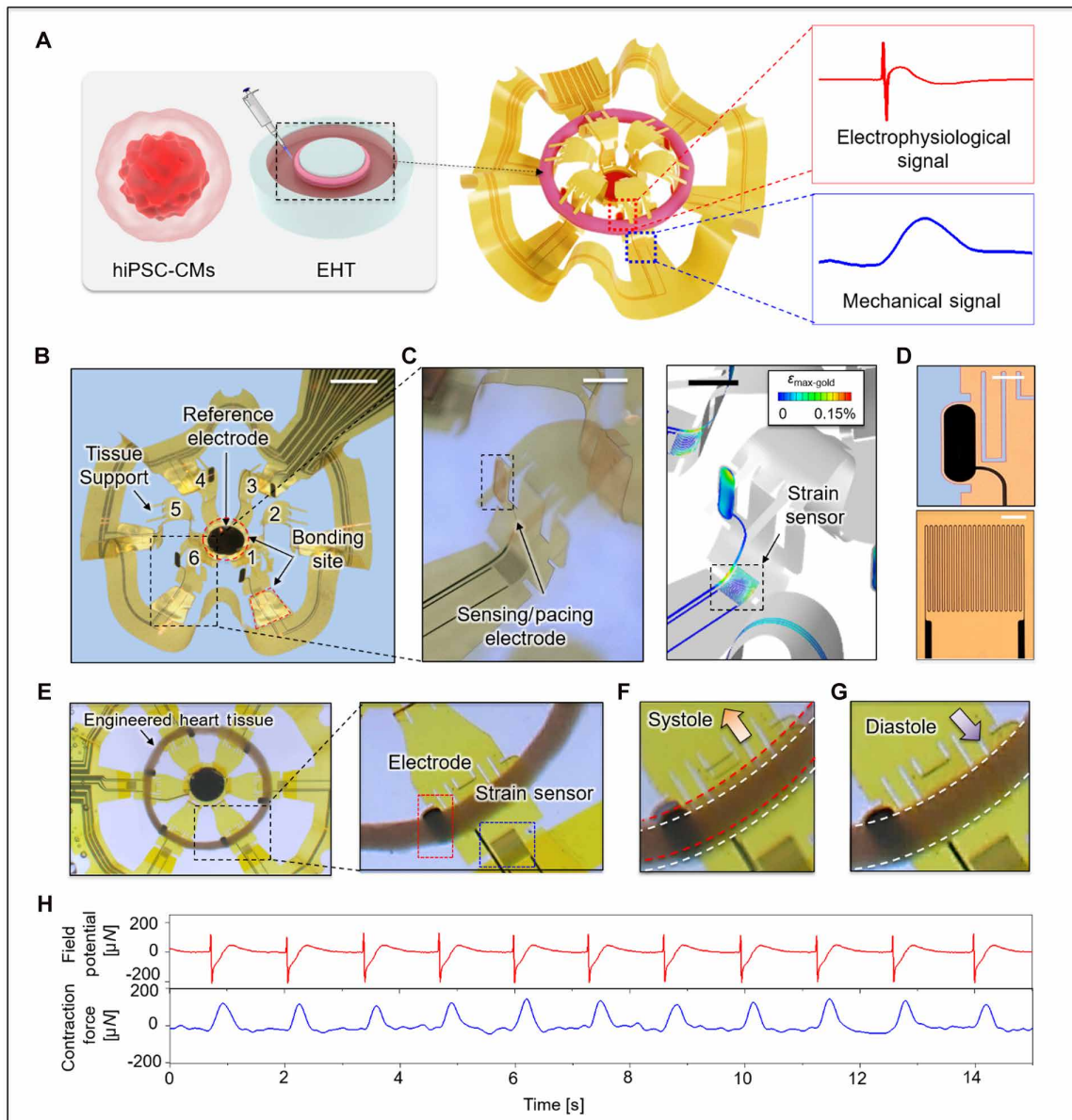
Fig. 1. Flexible 3D-MMF with EHT for spatiotemporal pacing and monitoring of electrophysiological and mechanical signals. (**A**) Schematic illustration of formation of ring-shaped EHTs and their integration with a 3D-MMF. (**B**) Configuration of the 3D-MMF that includes six instrumented post structures and a reference electrode. The red dotted box highlights one of the bonding sites used in constructing the 3D structure (scale bar, 2 mm). (**C**) Exposed Au electrode for electrophysiological sensing and pacing (scale bar, 1 mm, left) and for strain sensing (scale bar, 1 mm, right). (**D**) Optical image of a Pt-coated electrode (scale bar, 300 μm) and Au serpentine traces that define a strain sensor (scale bar, 100 μm). (**E**) Optical images of an EHT integrated with a 3D-MMF and a magnified view of an interface between electrode and EHT. Images showing deformations associated with (**F**) systole and (**G**) diastole. (**H**) Representative time synchronized field potential (red) and contraction force (blue) signal over a 15-s recording.

RHS Stim/Recording controller with I/O expander; Intan Technology) capable of simultaneously capturing local tissue field potentials and tissue contractile dynamics from spontaneously contractive cardiac tissue. A separate optical recording setup precisely captures displacements of the EHTs through a microscope (Fig. 2A) for validating the responses of the strain gauges. Figure 2B shows the positioning of the six electrodes (E1 to E6), the six strain sensors (S1 to S6), and the reference electrode. Figure 2 (C and D) displays consistent field potentials and contractile waveforms. The signal to noise can be further improved by signal averaging a series of contractions (shown here for a 1-s interval, with ~30 cycles of activity). The potentials are ~±200 μV, and the corresponding forces have amplitudes of ~150 μN. Information on the conduction propagation and dynamic activity follow from recordings at sampling rates of 20 kHz from each of the six symmetrically positioned posts (Fig. 2, E and H). The time between electrical activation and peak systolic force
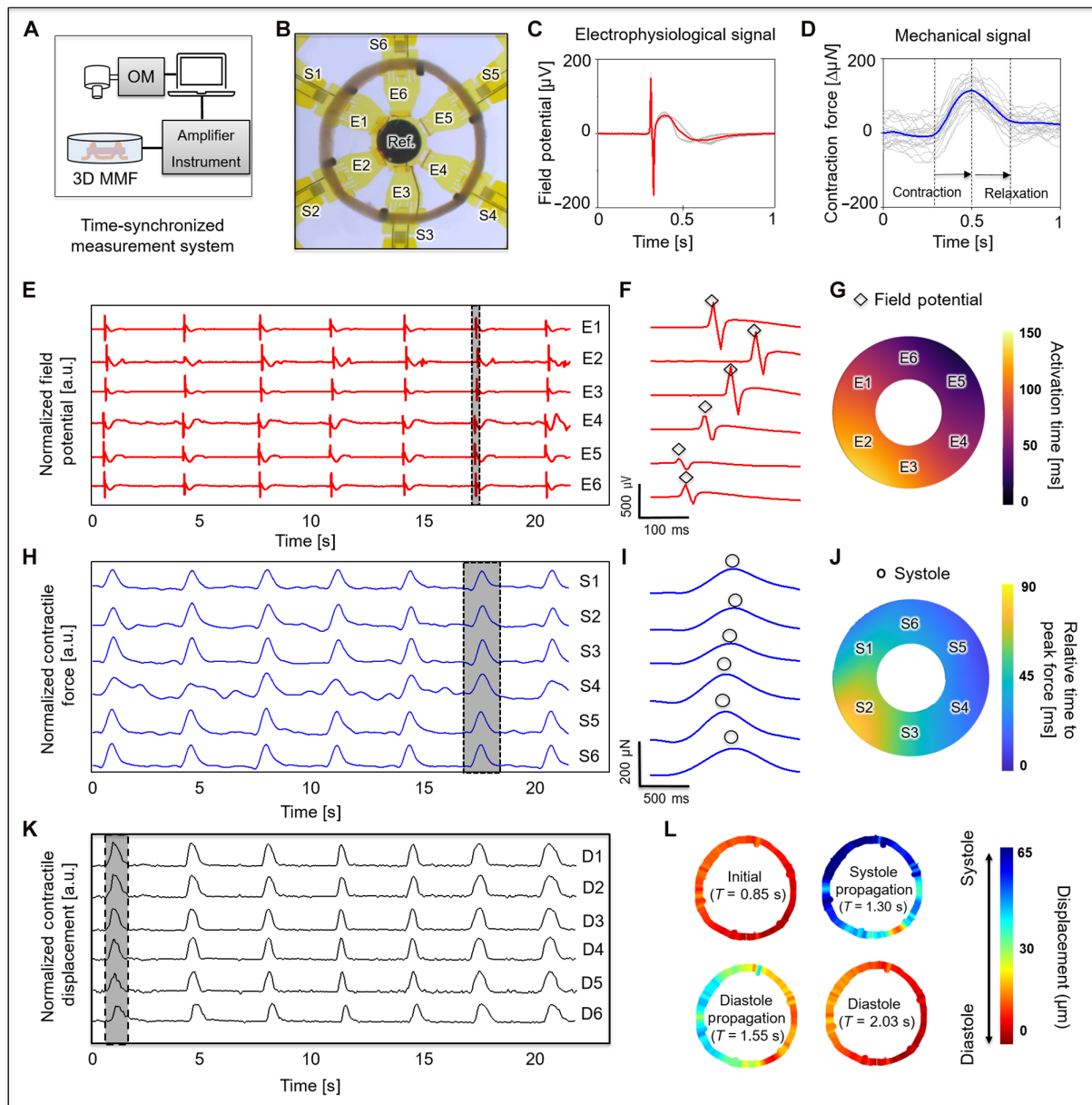
Fig. 2. Spatiotemporal, time-synchronized monitoring of electrophysiological and mechanical signals across EHTs in ring geometries. (**A**) Schematic diagram of the electronics for time-synchronized optical, electrophysiological, and mechanical measurements. (**B**) Optical micrograph that shows a labeled map of six post structures that serve as a 3D-MMF for the EHTs, with six strain sensors (S1 to S6), six electrodes (E1 to E6), and a round reference electrode. (**C**) Representative overlaid plots of electrophysiological recordings from 30 consecutive cycles of activity at electrode 1. (**D**) Representative overlaid plots of force recordings from 30 consecutive cycles of activity at strain sensor 1. (**E**) Representative electrophysiological recordings (red) at all electrode sites. (**F**) Plots of potentials that correspond to the region highlighted with the dashed rectangle in (E) (◇ R peak). (**G**) Electrical activation times that reveal propagation of the field potential. (**H**) Representative recordings of contractile force (blue) at all strain sensor sites. (**I**) Plots of force that correspond to the region highlighted with the dashed rectangle in (H) (○ maximum systole point). (**J**) Relative time to the peak of systolic force. (**K**) Systolic radical displacement (black) determined optically and correspondence to data collected with the strain sensors, and (**L**) deformation fields of a cycle at representative instants (initial at $T = 0.85$ s, systole propagation at $T = 1.30$ s, diastole propagation at $T = 1.55$ s, and diastole at T = 2.03 s).

generation (time to peak) is ~400 ms (Fig. 2, F and I), and the half-relaxation time is ~220 ms. The field potential measurements shown in Fig. 2F demonstrate bidirectional conduction propagation from a focus of automaticity that initiates near E5 and terminates near E2 ~150 ms later (Fig. 2G) with a conduction velocity of ~5.65 cm/s. The time delay of the propagation in mechanical systolic peak initiated by electrical activation is approximately 88 ms (Fig. 2J).

Displacement profiles determined optically at D1 to D6 exhibit trends similar to those of the strain signals at corresponding locations of S1 to S6 (Fig. 2K). The results indicate that the maximum displacement during systolic movement is 80 µm, corresponding to 106 µN (Fig. 2L and fig. S8). During this period, the strain sensor captures a force of 105 µN, with an average match rate across all locations of 88 ± 2%. Unlike traditional optical voltage or calcium

mapping approaches, which require inhibition of mechanical contraction, the EHT platform allows rapid, noninvasive measurements of both electrophysiologic and mechanical performance simultaneously across a single EHT over extended periods of observation.

Drug responses

A key aspect of hIPSC-CM derived EHTs is their utility for pharmacological assessment. Using our electromechanically monitored EHT platform, we assessed the electrophysiologic and contractile effects of drugs used clinically to augment or inhibit cardiac rhythm and function. Figure 3 (A and B) shows a representative response to the β-agonist isoproterenol (3 μM), demonstrating an increase in beat rate [beats per minute (BPM)] and in contractile force (*32*), mirroring human cardiac responses to these agents. Figure 3 (C to E) highlight the dose response of isoproterenol with respect to BPM, QT interval, and contractile force (average value from 30 peaks, data from three tissues). The stepwise increase in beat rate and contractile
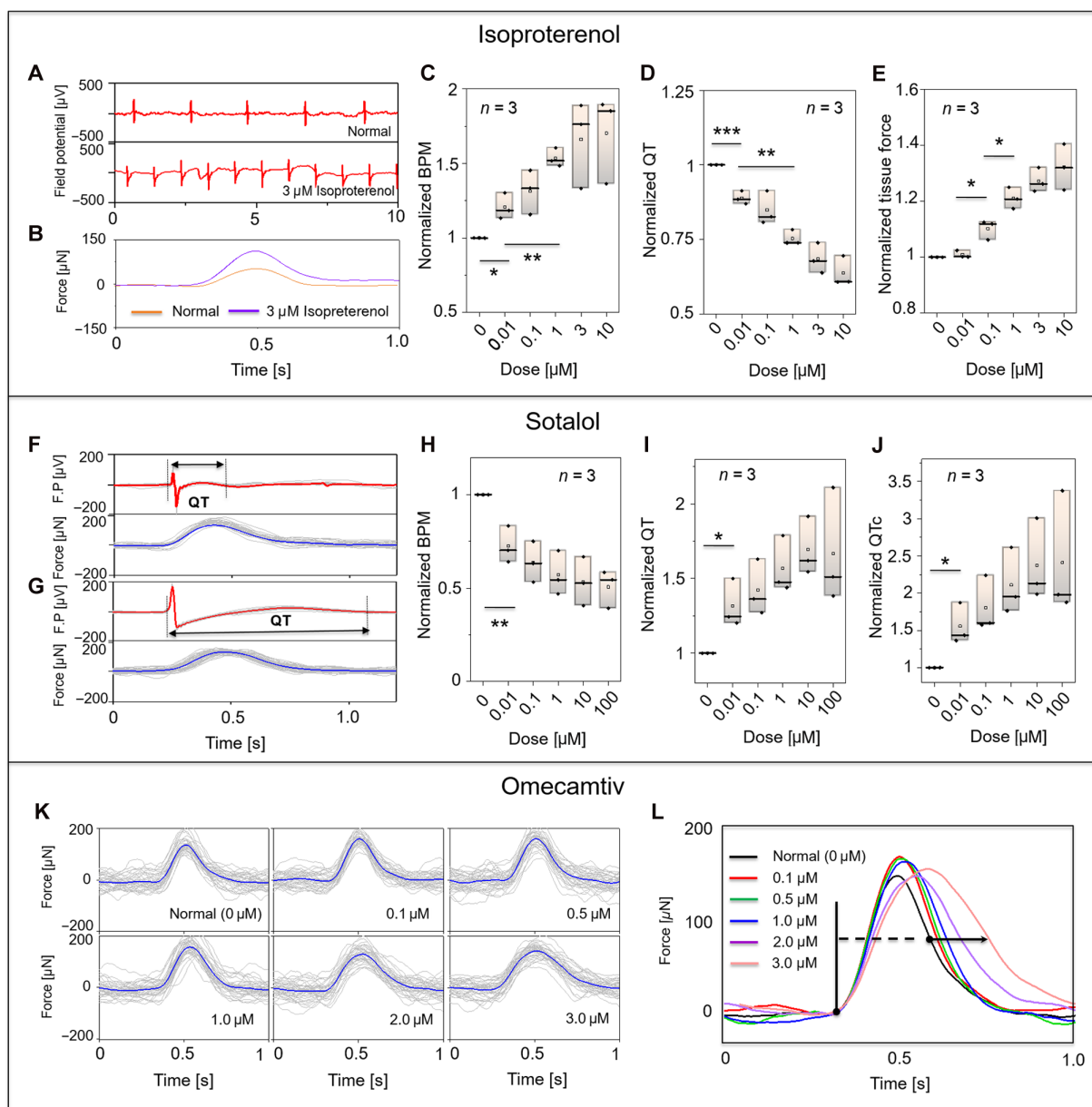

Fig. 3. Pharmacological manipulation of contractility and repolarization. (**A**) Representative field potential before and after introduction of isoproterenol (dose of 3 μM). (**B**) Overlaid plot of 30 cycles of contraction force before and after isoproterenol (dose of 3 μM), quantitative changes in (**C**) BPM, (**D**) QT interval, (**E**) contraction force with various concentrations of isoproterenol 0, 0.01, 0.1, 1, 3, and 10 μM. $n = 3$ tissues; *$P < 0.05$, **$P < 0.01$, and ***$P < 0.001$; one-way analysis of variance (ANOVA). Overlaid plot of 30 cycles of activity in field potential and contraction force in (**F**) untreated EHTs and (**G**) after introduction of sotalol (concentration of 10 μM). Quantitative changes in (**H**) BPM, (**I**) QT interval, and (**J**) QTc with various sotalol concentrations of 0, 0.01, 0.1, 1, 10, and 100 μM. (**K**) Overlaid plot of 30 averaged contraction cycles with different concentrations of omecamtiv (0, 0.1, 0.5, 1.0, 2.0, and 3.0 μM), and (**L**) comparison of representative averaged tissue force responses to each drug dose.

force with a concomitant reduction in the QT interval are all consistent with known in vivo human cardiac response to isoproterenol (*18, 33, 34*). We also assessed the effect of sotalol, a commonly used antiarrhythmic drug with both potassium channel and β-adrenergic–blocking activity. As shown in Fig. 3 (F and G), the QT interval significantly prolonged after 10 µM sotalol treatment (30 overlaid plots of field potentials). Figure 3 (H to J) shows the dose response curve for sotalol for BPM, QT, and corrected QT (QTc). Increasing sotalol leads to a stepwise decrease in the beat rate with the expected increase in the QT interval (*35, 36*). We also examined the effect of omecamtiv mecarbil, a myosin inhibitor studied in the GALATIC-HF trial (*37*). Omecamtiv is known to prolong systole (*38–40*), with a response that depends on loading conditions, even in EHTs (*32*). The average tissue response (Fig. 3K) shows a delayed time to peak with increasing omecamtiv dose (Fig. 3L), consistent with prior observations in hiPSC-CM EHTs (*32*). Together, these findings demonstrate successful simultaneous electromechanical monitoring of hiPSC-CM EHT drug responses to clinically relevant adrenergic and sarcomeric agents.

Pacing and stimulation and termination of reentrant arrhythmias

The MMF platform also provides an opportunity to study the effects of tissue stimulation, both nonterminally and noninvasively, without the need for contamination-prone field effect electrodes or tissue-penetrating contact electrodes. Each electrode within the 3D-MMF can also serve as a pacing electrode, as shown in Fig. 4A. In this case, electrode 2 stimulates the EHT for 30 s at a frequency of 60 bpm (300 µs, 200 µA, biphasic pulse) while the electrical and mechanical response is monitored at electrode 5 and strain sensor 5. After fast pacing ceases, the slower automatic rhythm resumes as expected. Figure 4B displays a typical period of field potential and conduction propagation in a circular array. EHTs are known to occasionally exhibit spontaneously reentrant rhythms (*18*), which we also observed (Fig. 4C) with minimal mechanical deflection due to the dyssynchronous contraction. As in the clinical setting, reentrant rhythms are sustainable when the wavelength (refractory period × conduction velocity) is shorter than the path length, or alternatively said, an excitable gap is present between the wavefront front and wave tail.
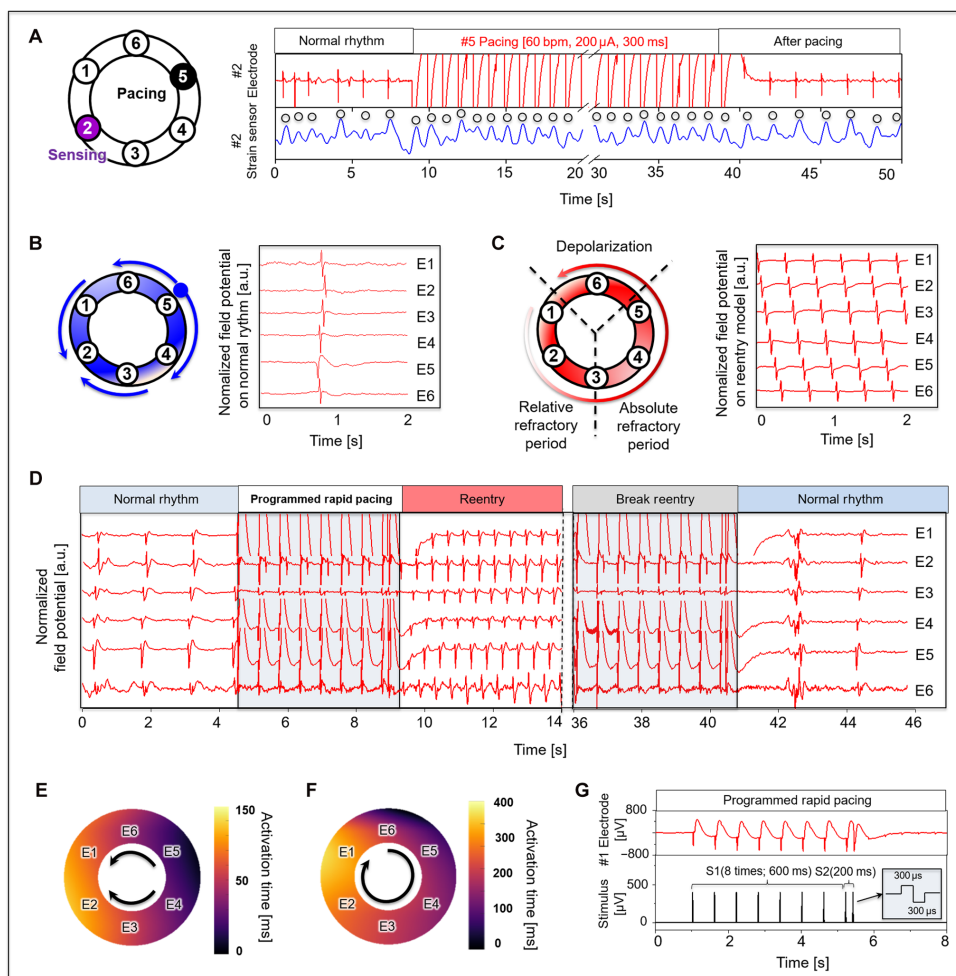

Fig. 4. Pacing, reentry, and electrical cardioversion in EHTs. (**A**) Observation of the field potential and contractile force at #2 post via applied pacing (60 bpm, 200 µA, 300 µs) at the #5 electrode on the opposite side. (**B**) Typical pattern of a normal rhythm of EHTs with a series of cycles propagating to both sides and terminating at a point. (**C**) Representative reentry circuit rhythm caused by delayed conduction velocity in one pathway. (**D**) An example of reversible reentry and cardioversion through rapid pacing. Activation time map on (**E**) normal rhythm and (**F**) reentry arrhythmias rhythm. (**G**) Programmed S1S2 electrical stimulation with biphasic waveform (amplitude of 400 µA and 300 µs of phase duration); cycle length of S1 (600ms) and S2 (200ms) with sequentially reduced (200 ms-*x*) final pacing interval.

Experiments that further leverage the pacing and the electrophysiologic and mechanical sensing capabilities of the EHT platform involve nonterminal studies to systematically induce and detect clinically relevant reentrant rhythms, without the need for membrane-sensitive dyes or toxic myosin inhibitors. The standard clinical protocol used on human hearts uses this same programmed electrical stimulation to induce reentrant rhythms (41). Figure 4D shows the induction of reentry in EHTs at a basic cycle length (BCL) of 600 ms (S1) with an S2 beat at 200 ms (Fig. 4G). Also shown in Fig. 4D, the reentrant rhythm terminates with rapid pacing. Figure 4E shows the activation map of the tissue under its spontaneous rhythm induced by an autonomic focus near E4. Conduction velocity, in this case, was ~8 cm/s. During reentry (Fig. 4F), the conduction velocity decreased markedly to ~4 cm/s, consistent with the expected conduction slowing at shorter cycle lengths. Reentry susceptibility increased with 25 μM pinacidil, which shortens the action potential duration. For some tissues, the excitable gap was too small with the path length close to the wavelength, such that a reentrant rhythm could not be induced.

DISCUSSION

Soft, biocompatible forms of electronics, especially those in 3D designs, that support sensors capable of monitoring biological processes have broad relevance in both clinical and research applications. This report substantially extends previously reported 3D-MMF technologies tailored to monitor electrical activity of neuronal organoids (23) and contraction of engineered skeletal muscle rings (42). The advances are in 3D framework designs tailored specifically to EHTs as both mechanical supports with well-defined loading conditions and as mounting sites for strain sensors and electrodes for both simulation and recording. The resulting technology enables continuous, simultaneous noninvasive monitoring of both field potentials and contraction dynamics at multiple locations in a precise, time-synchronized fashion. This EHT platform can noninvasively interrogate soft, mechanically active tissues, not only in circular ring geometries as demonstrated here but in other formats including strips or wedges. The noncompliant nature of conventional rigid electronics in standard 2D formats does not allow for adequate signal transduction in these contexts.

Over 100 years ago, Mines (43) first showed that reentrant rhythms could be developed in cardiac tissue and postulated a theoretical framework defining the requirements for initiation and maintenance of reentry. Garrey (44) also promoted the concept of a critical tissue mass for sustaining fibrillatory rhythms, highlighting the importance of tissue size or path length in reentry. Lewis later established that reentry was the mechanism of atrial fibrillation, which was further extended to ventricular fibrillation (45). Spontaneous reentrant rhythms have been observed in hiPSC-CM EHTs using optical mapping with voltage-sensitive membrane dyes in terminal experiments (18). While there are several alternatives for monitoring native action potentials with microelectrodes, voltage-sensitive membrane dyes, or genetically encoded transmembrane potential reporters, electromechanically monitored EHTs have the advantage of longer-term field potential monitoring, as a valuable proxy for clinically relevant parameters such as the repolarization interval (QTc) and conduction velocity. On the basis of our findings and the improved maturity of the electromechanically monitored EHT format, the EHT platform helps predict safety, arrhythmia

susceptibility, response to drugs, and serves as a platform for testing gene-directed therapeutic strategies. Because EHTs are generated from human cells, EHTs can be used to advance personalized treatments like "n of 1" antisense treatment or gene editing (46).

Electromechanically monitored EHTs are also useful for measuring conduction velocities. When comparing the tissue conduction velocity to the native myocardium, the EHTs in this study are comparable to others (~6 cm/s), but do not reach the longitudinal conduction velocities measured in the normal ventricular myocardium (~50 cm/s). The EHTs examined here have a path length of 15.7 mm (diameter of 5 mm), requiring the refractory period to be <~260 ms to sustain reentry. This value is, however, an estimate, due to tissue-to-tissue variability. Also, both conduction velocity and action potential duration decrease with decreasing cycle length, leading to a concomitant shortening of wavelength with an increase in pacing rate. As EHT formation methods improve to enhance cardiomyocyte maturity, intercellular connectivity, and incorporate additional cell types found in the human heart, conduction velocity and, therefore, wavelength will likely increase. Previous work on human heart wedge preparations demonstrated a longitudinal wavelength of ~10 cm at a BCL 250 ms (240 bpm). The addition of 25 μM pinacidil reduces the wavelength to ~5 cm at a BCL = 250 ms (240 bpm) and ~3 cm at BCL = 125 ms (480 bpm) (47). The ability to simulate reentry could be enhanced by increasing the circumferential path lengths of the tissues and devices. For EHTs that approach native myocardium conduction velocities, this path length requirement would be >~10 cm, which is 6.3× the length of our system. Alternatively, regional manipulation of EHT conduction velocity to slow conduction in a single tissue region is a viable alternative. While technically demanding, this approach may provide a feasible solution as larger tissue sizes will necessarily require increased hiPSC-CM input and considerable additional cost.

By comparison to other work examining reentry in an EHT format (18), this format has several key advantages. First, the MMF system eliminates the need for specialized optical equipment to track movements and allowing for parallelization of measurements across multiple tissues. Second, signals are monitored noninvasively without the need to remove the tissue from the incubator environment, thereby facilitating time-dependent and longer-term experiments. Third, experimental induction of reentry can be accomplished using the same techniques applied to patients undergoing EP studies, namely, S1S2 stimulation, in a way that avoids the mechanical manipulation of the fragile EHT tissue required with point electrode stimulation. Fourth, the MMF platform provides a ready mechanism to document arrhythmias without the need for toxic dyes and myosin inhibitors, as the field potential can be monitored from electrodes simultaneously. Together, the MMF platform serves a critical niche for the study of arrhythmia biology in hiPSC-CMs for both basic and translational applications.

3D flexible electronic frameworks coupled with human hiPSC-CM–derived EHTs form the basis of this electromechanically monitored EHT system, enabling immediate spatiotemporal observation and manipulation through noninvasive, continuous electrophysiological and mechanical means. Experiments presented here demonstrate that electromechanically monitored EHTs provide a potential for efficient disease modeling and developing and evaluating candidate pharmacological compounds. These multisensor platforms, as applied to circular EHT rings, offer the capability to measure many sites simultaneously and instantly, providing immediate observation of signal propagation and signal intensity for drug reactions and other forms of

stimulation. In particular, this system permits the study of cardiac tissue derived from a human genetic background, avoiding animal experiments. Also, each electrode can be used to deliver site-specific electrical stimulation to the tissue. EP studies on this MMF platform of ring-shaped EHTs demonstrate reentry rhythms, underscoring the ability to model human arrhythmias. This concept extends beyond the monitoring of biological signals under physiological loading conditions in EHTs to other forms of engineered soft tissues. These approaches thus have potential to improve the development of treatment options and drugs by integration with disease models.

MATERIALS AND METHODS
Fabrication of the 2D precursor
Techniques in photolithography and related methods in microfabrication yielded multilayered, flexible 2D precursors to the 3D-MMFs. The process began with spin coating (3000 rpm for 40 s) and baking (180°C for 150 s) of poly(methyl methacrylate) (PMMA) on a glass slide, followed by spin coating (1000 rpm for 40 s) and baking (120°C for 120 s, 150°C for 120 s, and 260°C for 1 hour with vacuum) of PI (PI-2545, HD Microsystems). A maskless aligner (MLA150, Heidelberg Instruments) defined patterns of a negative photoresist (AZ nLOF 2035) spin cast (5000 rpm for 40 s) and baked (110°C for 60 s). Postbaking (110°C for 90s) after photo exposure prepared the resist for development (immersion AZ MIF300 for 35 s) and rinsing with distilled water. Electron beam evaporation defined a thin, uniform layer of chrome (10 nm) and gold (200 nm), for lift off by immersion in a stripper (AZ400T, overnight). Spin coating and baking defined an encapsulating layer of PI on these patterned traces of Cr/Au. Patterning of a thin layer of copper (50 nm) deposited by sputtering on top of the PI involved first forming a layer of positive photoresist (S1805) by spin-casting (4000 rpm for 40 s) and baking (110°C for 60 s). Exposing the resist with a maskless aligner followed by immersion in a developer (AZ 917 for 30 s) exposed regions of the PI for removal by exposure to an oxygen plasma etching (220 mT, 200 W, 60 min). Immersion in a copper etchant diluted with distilled water (ratio of 10:1) for 2 s removed the copper hard mask. Rising in distilled water completed the fabrication.

Assembly of 3D MEA with electronics
Immersion in acetone for 30 min removed the sacrificial underlayer of PMMA, to allow release of the 2D precursor from the glass substrate. Transfer of the precursor onto a water-soluble polyvinyl alcohol (PVA) tape allowed exposure of the backside for patterning bonding sites by deposition through a shadow mask of PI. These sites consisted of Ti (10 nm)/SiO$_2$ (50 nm) formed by electron beam evaporation through a shadow mask. Contact with a prestretched elastomer substrate (Dragon skin 10 medium, Smooth-On) after exposing both the elastomer and the backside of the 2D precursor to an ultraviolet plasma for 4 min activated the surface. Bringing these two elements into contact followed by heating to 70°C for 10 min formed strong covalent linkages at the bonding locations.

Dissolving the PVA tape in distilled water, and release of the prestretched elastomer, led to the formation of a 3D structure via mechanical buckling. A medical-grade silicone adhesive (Kiwk-sil, World Precision Instrument) bonded a well structure formed in PDMS to the elastomer substrate at distance slightly beyond the perimeter of the 3D-MMF. Interconnect contact pads served as an interface to a printed circuit board via anisotropic conductive film cables. A coating of Pt black on the electrodes resulted from electrodeposition controlled by a potentiostat (Autolab PGSTAT128N, Metrohm AG) in a three-electrode configuration (−0.1 V for 60 s) with a Pt wire as a counter electrode and Ag/AgCl as a reference electrode in a Pt solution (3 wt % of chloroplatinic acid and 0.1 wt % of lead acetate). The surface morphology of the Pt black was observed by field-emission scanning electron microscopy (S-3400N, Hitachi, Japan) (fig. S4). The impedance was measured in a PBS (pH 7.4) with a frequency range from 1 Hz to 1 mHz (fig. S5). All samples were sterilized using an autoclave at 124°C for 1 hour. Additional sterilization involved exposure to ultraviolet light for 30 min and to EtOH before mounting the EHTs on the device.

Determination of forces from strain gauge measurements
The output voltage of the Wheatstone bridge V_0 follows

$$V_0 = V_{DD}\left(\frac{R_1}{R_1 + R_2} - \frac{R_0}{R_0 + R_3}\right) \tag{1}$$

where V_{DD} is the applied voltage, R_0 is initial resistance of the strain gauge, $R_{1,2}$ are fixed 1-megohm resistors, and R_3 is a potentiometer for controlling bias voltage (fig. S6). As cardiac activation induces bending of a post, and its associated strain gauge, the resistance changes to R_0', and the output voltage change is $\Delta V_0 = V_{DD}\left(\frac{R_0}{R_0 + R_3} - \frac{R_0'}{R_0' + R_3}\right)$. Simplifying this formula with $\Delta R = \left(R_0 - R_0'\right)$ yields an equation for the relative resistance change as below

$$\Delta V_0 = V_{DD}\frac{R_0 R_3 - R_0' R_3}{\left(R_0 + R_3\right)\left(R_0' + R_3\right)}$$
$$= V_{DD}\frac{\Delta R}{\left(\frac{R_0}{R_3} + 1\right)\left(\frac{R_0'}{R_3} + 1\right)R_3} \approx \frac{V_{DD}\Delta R}{4R_3} \tag{2}$$

$$\left(\because \frac{\Delta R}{R_3} \ll \frac{R_0'}{R_3} + 1\right) \tag{3}$$

$$\frac{\Delta R}{R_0} = \frac{4R_3\Delta V_0}{V_{DD}R_0} \tag{4}$$

Quantitative relationships between the contraction force of the EHT and the change in output voltage follow from measurements of the gauge factors of the strain sensors using direct, nanoindentation (Hysitron Biosoft Indenter, Bruker, USA) tests. Measurement of the indentation force involved 10 repeated linear cycles with a cross-head speed of 20 μm/s and displacement ranging from 0 to 160 μm. Recording changes in the output voltage of the strain sensor established correlations to the deformations of the post. Experiments under uniaxial indentation indicate linear responses with gauge factors of $15.7x \times 0.04$ (fig. S8).

Culturing hiPSC-CMs, forming EHTs, and transfer to 3D-MMFs
Control hiPSCs GM03348 [healthy male, Corriel, previously reprogrammed (48)] and SCVI2372 (healthy male, Stanford SCVI Biobank) were cultured and differentiated into hiPSC-CMs using methods described elsewhere (49), which are derived from the protocols of Burridge et al. (50) and Buikema et al. (31). EHTs were created by combining 90% hiPSC-CMS with 10% human cardiac fibroblasts (Promocell, C-12375) and embedding in a collagen-based hydrogel per prior methods (30, 51) with the modification of an increase in the total number of cells per EHT to 750,000 from 500,000 (total volume of 180 μl). Tissues are cast on custom

fabricated circular PMDS molds. Tissues are allowed to gel for 1 hour at 37 C, after which they were cultured in 10% horse serum (Gibco, 26050088), 1% penicillin/streptomycin, and 0.1% insulin in low-glucose Dulbecco's minimum essential medium (Sigma-Aldrich, D5546) with media exchanged on a Monday-Wednesday-Friday schedule. For the first 3 days of culture, transforming growth factor–β1 (5 ng/ml; Peprotech 100-21C) was added to improve EHT remodeling and consolidation per prior reports (*12*, *30*). After 1 week of culture, EHTs are washed with calcium- and magnesium-free PBS (Gibco, 14190144) and then treated with 30 μM *N*-benzyl-*p*-toluenesulfonamide (TCI, B3082) to inhibit tissue contraction for 5 min. The tissues were then gently lifted of the PDMS posts with the blunt side of forceps and transferred to the previously prepared flexible electronic. The unique layout matches requirements for use with the ring-shaped EHTs reported here, with inward slanting cantilever post design with an upper support structure to stabilize the tissue and ensure firm contact between the tissue and the electrodes. Media is exchanged for the EHT culture media and tissues were maintained for downstream studies.

Quantifying cell loading conditions

The cell loading conditions in length and geometry provided by a commercial tissue support structure with a traditional 2-post format are in fig. S11. The following describes a general approach to characterize auxotonic tissue loading conditions for 3D-MMFs with an arbitrary number of posts.

The following equation defines the auxotonic loading of the tissue

$$sF_{\text{tis}} = K\left(\Delta L_{\text{tis}} / L_{\text{tis}}\right) \tag{5}$$

where sF_{tis} is the circumferential force of the tissue normalized to cell/length or equivalently to cross-sectional area, K is the loading constant of the tissue, ΔL_{tis} is the change in the circumferential length from the resting length, and L_{tis} is the circumferential resting (diastolic) length of the tissue

$$sF_{\text{tis}} = F_{\text{tis}} / CD \tag{6}$$

where F_{tis} is the circumferential tissue force, and CD is the cell density (cells per unit length). When K is equal between arbitrary tissue geometries, cross-sectional areas, and lengths, then the auxotonic tissue load is equivalent. Figure S11 shows free body diagrams for the two specific cases of interest, the 2-post commercial device and the 6-post 3D-MMF.

The equation for the 2-post case is summarized as follows

$$\Delta L_{\text{pp}} = \Delta L_{\text{tis}} / 2 \tag{7}$$

$$F_{\text{post}} = K_{\text{post}} \times \Delta L_{\text{pp}} / 2 \tag{8}$$

$$F_{\text{post}} = K_{\text{post}} \times \Delta L_{\text{tis}} / 4 \tag{9}$$

Summing the forces along the y axis, yields the following

$$\sum Fy = 0 = -2F_{\text{tis}} + F_{\text{post}}$$
$$\therefore F_{\text{post}} = 2F_{\text{tis}} \tag{10}$$

$$F_{\text{tis}} = K_{\text{post}} \times \Delta L_{\text{tis}} / 8 \tag{11}$$

Rearranging yields

$$F_{\text{tis}} = K\left(\Delta L_{\text{tis}} / L_{\text{tis}}\right)(8 \times CD) \tag{12}$$

The equation for the 6-post 3-MMF is summarized as follows

$$\sum F_{\text{y}} = 0 = -2F_{\text{tis}} + 2\sin\left(60^{°}\right)F_{\text{post}} \Rightarrow F_{\text{tis}} = \sqrt{3}/2 \times F_{\text{post}} \tag{13}$$

$$L_{\text{tis}} = 2\pi r_{\text{d}} \Rightarrow \Delta L_{\text{tis}} = 2\pi\Delta r \tag{14}$$

Where Δr is the diastole radius (r_{d}) minus the systole radius (r_{s}). The following relationship therefore holds

$$F_{\text{post}} = k_{\text{post}} \times \Delta r = k_{\text{post}} \times \Delta L_{\text{tis}} / 2\pi \tag{15}$$

Then, combining from above

$$F_{\text{tis}} = \left(\sqrt{3}/4\pi\right) \times k_{\text{post}} \times \Delta L_{\text{tis}} = K\left(\Delta L_{\text{tis}}/L_{\text{tis}}\right)$$
$$CD = \left(\sqrt{3}/4\pi\right) \times k_{\text{post}} \times \Delta L_{\text{tis}} \tag{16}$$

And therefore K for the 6-post 3D-MMF is the following

$$K = \left(\sqrt{3}/2\right) \times k_{\text{post}} \times L_{\text{tis}} / (2\pi \, CD) \tag{17}$$

The contraction force information from the commercially available 2-post Myriamed system is as follows

$$\begin{aligned} &L_{\text{tis}} = 10 \text{ mm} \\ &CD = \text{Cell density } 500{,}000 \text{ cells}/10 \text{ mm} = 50{,}000 \text{ cells/mm} \\ &k_{\text{post}} = \text{TM4}: 0.7 \text{ mN/mm, TM5}: 1.5 \text{ mN/mm,} \\ &\qquad\quad \text{TM6}: 2.4 \text{ mN/mm, TM7}: 3.3 \text{ mN/mm} \end{aligned} \tag{18}$$

$$\begin{aligned} &K = L_{\text{tis}} \times k_{\text{post}}/(8 \times CD) \\ &K = \text{TM4}: 1.75 \times 10^{-5} \text{ mN mm cells}^{-1}, \\ &\qquad\; \text{TM5}: 3.75 \times 10^{-5} \text{ mN mm cells}^{-1}, \\ &\qquad\; \text{TM6}: 6.00 \times 10^{-5} \text{ mN mm cells}^{-1}, \\ &\qquad\; \text{TM7}: 8.25 \times 10^{-5} \text{ mN mm cells}^{-1} \end{aligned} \tag{19}$$

The contraction force calculation of the 6-post 3D MMF system is as follows

$$\begin{aligned} &L_{\text{tis}} = \pi \, 4.4 \text{ mm} = 13.816 \text{ mm} \\ &CD = \text{Cell density } 750{,}000 \text{ cells}/13.816 \text{ mm} = 54{,}284 \text{ cells/mm} \\ &k_{\text{post}} = 1.32 \text{ mN/mm (from measured stiffness)} \end{aligned}$$

$$\begin{aligned} K &= \left(\sqrt{3}/4\pi\right) \times k_{\text{post}} \times L_{\text{tis}} / CD \tag{20} \\ &= \left(\sqrt{3}/4\pi\right) \times 1.32 \text{ mN/mm} \times 13.8 \text{ mm}/(50{,}666 \text{ cells/mm}) \\ K &= 4.63 \times 10^{-5} \text{ mN mm cells}^{-1} \end{aligned}$$

Therefore, the loading conditions into the 3D MMF ($K = 4.63 \times 10^{-5}$ mN mm cells^{-1}) are similar to the EHT created on the commercial Myriamed system (TM5: 3.75×10^{-5} mN mm cells^{-1}).

Signal acquisition and data processing

A commercial amplifier system (INTAN 128 ch RHS Stim/Recording controller with I/O expander, Intan Technology) and its

associated software (Intan RHX) served as the data acquisition platform for the time-synchronized recording of electrophysiological and mechanical responses of the EHT in a 37°C incubator (fig. S14). The RHS2116 amplifier chip allowed collection of electrophysiological data with 16-bit resolution at a sampling rate of 20 kHz by linking to a digital port. The strain gauges yielded changes in output voltage captured through an instrument amplifier (INA322, Texas Instrument) with a gain of 1000× from a quarter Wheatstone bridge circuit. A hardware low-pass filter was connected to analog ports for recording. In addition, real-time display capabilities allowed for immediate monitoring and data visualization. The raw data were processed using a digital band-stop filter constructed in MATLAB ranging from 59.5 to 60.5 Hz and a digital high-pass filter having cutoff frequency of 300 Hz. An inherent peak finding function in MATLAB defined electrophysiological peaks with minimum peak intervals of 500 ms and a threshold of 80% value from minimum to maximum for each peak. These peak indexes served as criteria for overlapping both electrophysical and mechanical signals from EHT in the MATLAB script, allowing for overlap of 30 peaks with minimal artifacts.

Optical video analysis

A custom optical tracking method quantified the deformation fields of EHTs and validated the correlated mechanical contraction signals from the 3D-MMF. The experiments used a camera (Motic SMZ-171 head and Motic Moticam 1080BHM, Motic, Canada) with a resolution of 1920 × 1080 pixels at 25 fps, mounted perpendicular to the sensor. The tracking method consisted of three steps. First, the image sequence was converted into a binary sequence using the Renyi Entropy method, where the pixel values representing the EHT were set to 255, while the background was set to 0. Second, the sectional area of the EHT with respect to angle ($\Delta\theta = 1 \pm 3°$) was tracked in the spatiotemporal domain (*52*). Last, the deformation fields were quantified by tracking the radial distance of the angular area over time. Movie S2 shows the overall process of the optical method.

Pharmacological responses on EHT

Pharmacologic studies were performed between week ~3 of EHT culture. In some cases, the same tissues were used for pharmacologic testing, in which case >48 hours of drug wash out was allowed. Stock solutions were prepared and diluted to the specified concentration in EHT media. Stock solutions were as follows: 10 mM isoproterenol (Sigma-Aldrich, I5627) in deionized water, 100 mM sotalol (Sigma-Aldrich, PHR2798) in dimethyl sulfoxide (DMSO), and 10 mM omecamtiv (Cayman Chemical, 21074) in DMSO. Dose response curves were obtained by incubating different concentrations of isoproterenol (0, 0.01, 0.1, 1, 3, and 10 μM), sotalol (0, 0.01, 0.1, 1, 10, and 100 μM), and omecamtiv (0, 0.1, 0.5, 1.0, 2.0, and 3.0 μM) in a stepwise fashion. Tissues were equilibrated for 20 min at each concentration in the incubator before measuring the tissue response.

Rapid pacing for EP study

For programmable S1S2 stimulation, a 2-ch oscilloscope/waveform generator (Analog Discovery 2, Digilent) was connected to the input terminal of the Intan Stimulating/Recorder, which was programmed to follow the output of the Analog Discovery 2 waveform generator that was programmed to produce a standard S1S2 stimulation protocol. The stimulation protocol involves eight cycles of S1 stimulation with an adjustable BCL and the S2 stimulation follows the last S1 stimulation in a stepwise manner with an adjustable S2 cycle length. The biphasic stimulus has a phase duration of 300 μs and an amplitude 400 μA. The cycle length of S2 is adjusted while recording the patterns of the six field potentials in real time.

Supplementary Materials

The PDF file includes:
Supplementary Text
Figs. S1 to S15
Legends for movies S1 to S4
Legends for data S1 to S5
References

Other Supplementary Material for this manuscript includes the following:
Movies S1 to S4
Data S1 to S5

REFERENCES AND NOTES

1. B. Yu, S. R. Zhao, C. D. Yan, M. Zhang, J. C. Wu, Deconvoluting the cells of the human heart with iPSC technology: Cell types, protocols, and uses. *Curr. Cardiol. Rep.* **24**, 487–496 (2022).
2. P. W. Burridge, A. Holmström, J. C. Wu, Chemically defined culture and cardiomyocyte differentiation of human pluripotent stem cells. *Curr. Protoc. Hum. Genet.* **87**, 21.3.1–21.3.15 (2015).
3. S. R. Houser, K. B. Margulies, A. M. Murphy, F. G. Spinale, G. S. Francis, S. D. Prabhu, H. A. Rockman, D. A. Kass, J. D. Molkentin, M. A. Sussman, W. J. Koch; American Heart Association Council on Basic Cardiovascular Sciences, Council on Clinical Cardiology, and Council on Functional Genomics and Translational Biology, Animal models of heart failure: A scientific statement from the American Heart Association. *Circ. Res.* **111**, 131–150 (2012).
4. K. Nakao, W. Minobe, R. Roden, M. R. Bristow, L. A. Leinwand, Myosin heavy chain gene expression in human heart failure. *J. Clin. Invest.* **100**, 2362–2370 (1997).
5. S. Schiaffino, A. C. Rossi, V. Smerdu, L. A. Leinwand, C. Reggiani, Developmental myosins: Expression patterns and functional significance. *Skelet. Muscle* **5**, 22 (2015).
6. J. Montag, B. Petersen, A. Flögel, E. Becker, A. Lucas-Hahn, G. Cost, C. Mühlfeld, T. Kraft, H. Niemann, B. Brenner, Successful knock-in of hypertrophic cardiomyopathy-mutation R723G into the MYH7 gene mimics HCM pathology in pigs. *Sci. Rep.* **8**, 4786 (2018).
7. M. Wadman, FDA no longer has to require animal testing for new drugs. *Science* **379**, 127–128 (2023).
8. J. J. Han, FDA Modernization Act 2.0 allows for alternatives to animal testing. *Artif. Organs* **47**, 449–450 (2023).
9. N. Sayed, C. Liu, J. C. Wu, Translation of human-induced pluripotent stem cells: From clinical trial in a dish to precision medicine. *J. Am. Coll. Cardiol.* **67**, 2161–2176 (2016).
10. C. Tu, B. S. Chao, J. C. Wu, Strategies for improving the maturity of human induced pluripotent stem cell-derived cardiomyocytes. *Circ Res*. **123**, 512–514 (2018); https://doi.org/10.1161/CIRCRESAHA.118.313472.
11. I. Karakikes, M. Ameen, V. Termglinchan, J. C. Wu, Human induced pluripotent stem cell–derived cardiomyocytes: Insights into molecular, cellular, and functional phenotypes. *Circ. Res.* **117**, 80–88 (2015).
12. M. Tiburcy, J. E. Hudson, P. Balfanz, S. Schlick, T. Meyer, M.-L. C. Liao, E. Levent, F. Raad, S. Zeidler, E. Wingender, J. Riegler, M. Wang, J. D. Gold, I. Kehat, E. Wettwer, U. Ravens, P. Dierickx, L. W. van Laake, M. J. Goumans, S. Khadjeh, K. Toischer, G. Hasenfuss, L. A. Couture, A. Unger, W. A. Linke, T. Araki, B. Neel, G. Keller, L. Gepstein, J. C. Wu, W.-H. Zimmermann, Defined engineered human myocardium with advanced maturation for applications in heart failure modeling and repair. *Circulation* **135**, 1832–1847 (2017).
13. K. Breckwoldt, D. Letuffe-Brenière, I. Mannhardt, T. Schulze, B. Ulmer, T. Werner, A. Benzin, B. Klampe, M. C. Reinsch, S. Laufer, A. Shibamiya, M. Prondzynski, G. Mearini, D. Schade, S. Fuchs, C. Neuber, E. Krämer, U. Saleem, M. L. Schulze, M. L. Rodriguez, T. Eschenhagen, A. Hansen, Differentiation of cardiomyocytes and generation of human engineered heart tissue. *Nat. Protoc.* **12**, 1177–1197 (2017).
14. J. Schwan, A. T. Kwaczala, T. J. Ryan, O. Bartulos, Y. Ren, L. R. Sewanan, A. H. Morris, D. L. Jacoby, Y. Qyang, S. G. Campbell, Anisotropic engineered heart tissue made from laser-cut decellularized myocardium. *Sci. Rep.* **6**, 32068 (2016).
15. I. Mannhardt, K. Breckwoldt, D. Letuffe-Brenière, S. Schaaf, H. Schulz, C. Neuber, A. Benzin, T. Werner, A. Eder, T. Schulze, B. Klampe, T. Christ, M. N. Hirt, N. Huebner, A. Moretti,

T. Eschenhagen, A. Hansen, Human engineered heart tissue: Analysis of contractile force. *Stem Cell Reports* **7**, 29–42 (2016).

16. J. M. Bliley, M. Vermeer, R. M. Duffy, I. Batalov, D. Kramer, J. W. Tashman, D. J. Shiwarski, A. Lee, A. S. Teplenin, L. Volkers, B. Coffin, M. F. Hoes, A. Kalmykov, R. N. Palchesko, Y. Sun, J. D. H. Jongbloed, N. Bomer, R. A. de Boer, A. J. H. Suurmeijer, D. A. Pijnappels, M. C. Bolling, P. van der Meer, A. W. Feinberg, Dynamic loading of human engineered heart tissue enhances contractile function and drives a desmosome-linked disease phenotype. *Sci. Transl. Med.* **13**, eabd1817 (2021).

17. M. Kim, J. C. Hwang, S. Min, Y.-G. Park, S. Kim, E. Kim, H. Seo, W. G. Chung, J. Lee, S.-W. Cho, J.-U. Park, Multimodal characterization of cardiac organoids using integrations of pressure-sensitive transistor arrays with three-dimensional liquid metal electrodes. *Nano Lett.* **22**, 7892–7901 (2022).

18. I. Goldfracht, S. Protze, A. Shiti, N. Setter, A. Gruber, N. Shaheen, Y. Nartiss, G. Keller, L. Gepstein, Generating ring-shaped engineered heart tissues from ventricular and atrial human pluripotent stem cell-derived cardiomyocytes. *Nat. Commun.* **11**, 75 (2020).

19. N. V. Chavali, D. O. Kryshtal, S. S. Parikh, L. Wang, A. M. Glazer, D. J. Blackwell, B. M. Kroncke, M. B. Shoemaker, B. C. Knollmann, Patient-independent human induced pluripotent stem cell model: A new tool for rapid determination of genetic variant pathogenicity in long QT syndrome. *Heart Rhythm* **16**, 1686–1695 (2019).

20. W. Dou, A. Daoud, X. Chen, T. Wang, M. Malhi, Z. Gong, F. Mirshafiei, M. Zhu, G. Shan, X. Huang, Ultrathin and flexible bioelectronic arrays for functional measurement of iPSC-cardiomyocytes under cardiotropic drug administration and controlled microenvironments. *Nano Lett.* **23**, 2321–2331 (2023).

21. H. Chen, B. Jiang, J. G. Shamul, X. He, Image entropy-based label-free functional characterization of human induced pluripotent stem cell-derived 3D cardiac spheroids. *Biosens. Bioelectron.* **179**, 113055 (2021).

22. Z. Xie, R. Avila, Y. Huang, J. A. Rogers, Flexible and stretchable antennas for biointegrated electronics. *Adv. Mater.* **32**, e1902767 (2020).

23. Y. Park, C. K. Franz, H. Ryu, H. Luan, K. Y. Cotton, J. U. Kim, T. S. Chung, S. Zhao, A. Vazquez-Guardado, D. S. Yang, K. Li, R. Avila, J. K. Phillips, M. J. Quezada, H. Jang, S. S. Kwak, S. M. Won, K. Kwon, H. Jeong, A. J. Bandodkar, M. Han, H. Zhao, G. R. Osher, H. Wang, K. H. Lee, Y. Zhang, Y. Huang, J. D. Finan, J. A. Rogers, Three-dimensional, multifunctional neural interfaces for cortical spheroids and engineered assembloids. *Sci. Adv.* **7**, eabf9153 (2021).

24. Q. Huang, B. Tang, J. C. Romero, Y. Yang, S. K. Elsayed, G. Pahapale, T.-J. Lee, I. E. M. Pantoja, F. Han, C. Berlinicke, T. Xiang, M. Solazzo, T. Hartung, Z. Qin, B. S. Caffo, L. Smirnova, D. H. Gracias, Shell microelectrode arrays (MEAs) for brain organoids. *Sci. Adv.* **8**, eabq5031 (2022).

25. A. Kalmykov, C. Huang, J. Bliley, D. Shiwarski, J. Tashman, A. Abdullah, S. K. Rastogi, S. Shukla, E. Mataev, A. W. Feinberg, K. J. Hsia, T. Cohen-Karni, Organ-on-e-chip: Three-dimensional self-rolled biosensor array for electrical interrogations of human electrogenic spheroids. *Sci. Adv.* **5**, eaax0729 (2019).

26. Y. S. Choi, H. Jeong, R. T. Yin, R. Avila, A. Pfenniger, J. Yoo, J. Y. Lee, A. Tzavelis, Y. J. Lee, S. W. Chen, H. S. Knight, S. Kim, H.-Y. Ahn, G. Wickerson, A. Vázquez-Guardado, E. Higbee-Dempsey, B. A. Russo, M. A. Napolitano, T. J. Holleran, L. A. Razzak, A. N. Miniovich, G. Lee, B. Geist, B. Kim, S. Han, J. A. Brennan, K. Aras, S. S. Kwak, J. Kim, E. A. Waters, X. Yang, A. Burrell, K. S. Chun, C. Liu, C. Wu, A. Y. Rwei, A. N. Spann, A. Banks, D. Johnson, Z. J. Zhang, C. R. Haney, S. H. Jin, A. V. Sahakian, Y. Huang, G. D. Trachiotis, B. P. Knight, R. K. Arora, I. R. Efimov, J. A. Rogers, A transient, closed-loop network of wireless, body-integrated devices for autonomous electrotherapy. *Science* **376**, 1006–1012 (2022).

27. S. Xu, Z. Yan, K.-I. Jang, W. Huang, H. Fu, J. Kim, Z. Wei, M. Flavin, J. M. Cracken, R. Wang, A. Badea, Y. Liu, D. Xiao, G. Zhou, J. Lee, H. U. Chung, H. Cheng, W. Ren, A. Banks, X. Li, U. Paik, R. G. Nuzzo, Y. Huang, Y. Zhang, J. A. Rogers, Assembly of micro/nanomaterials into complex, three-dimensional architectures by compressive buckling. *Science* **347**, 154–159 (2015).

28. H. Ryu, Y. Park, H. Luan, G. Dalgin, K. Jeffris, H.-J. Yoon, T. S. Chung, J. U. Kim, S. S. Kwak, G. Lee, H. Jeong, J. Kim, W. Bai, J. Kim, Y. H. Jung, A. K. Tryba, J. W. Song, Y. Huang, L. H. Philipson, J. D. Finan, J. A. Rogers, Transparent, compliant 3D mesostructures for precise evaluation of mechanical characteristics of organoids. *Adv. Mater.* **33**, e2100026 (2021).

29. M. H. Drazner, The progression of hypertensive heart disease. *Circulation* **123**, 327–334 (2011).

30. M. Tiburcy, T. Meyer, N. Y. Liaw, W.-H. Zimmermann, Generation of engineered human myocardium in a multi-well format. *STAR Protoc.* **1**, 100032 (2020).

31. J. W. Buikema, S. Lee, W. R. Goodyer, R. G. Maas, O. Chirikian, G. Li, Y. Miao, S. L. Paige, D. Lee, H. Wu, D. T. Paik, S. Rhee, L. Tian, F. X. Galdos, N. Puluca, B. Beyersdorf, J. Hu, A. Beck, S. Venkamatran, S. Swami, P. Wijnker, M. Schuldt, L. M. Dorsch, A. van Mil, K. Red-Horse, J. Y. Wu, C. Geisen, M. Hesse, V. Serpooshan, S. Jovinge, B. K. Fleischmann, P. A. Doevendans, J. van der Velden, K. C. Garcia, J. C. Wu, J. P. G. Sluijter, S. M. Wu, Wnt activation and reduced cell-cell contact synergistically induce massive expansion of functional human iPSC-derived cardiomyocytes. *Cell Stem Cell* **27**, 50–63 e5 (2020).

32. A. Rhoden, T. Schulze, N. Pietsch, T. Christ, A. Hansen, T. Eschenhagen, Comprehensive analyses of the inotropic compound omecamtiv mecarbil in rat and human cardiac preparations. *Am. J. Physiol. Heart Circ. Physiol.* **322**, H373–H385 (2022).

33. S. H. Thomas, E. R. Behr, Pharmacological treatment of acquired QT prolongation and torsades de pointes. *Br. J. Clin. Pharmacol.* **81**, 420–427 (2016).

34. H. T. Dodge, J. D. Lord, H. Sandler, Cardiovascular effects of isoproterenol in normal subjects and subjects with congestive heart failure. *Am. Heart J.* **60**, 94–105 (1960).

35. E. G. Navarrete, P. Liang, F. Lan, V. Sanchez-Freire, C. Simmons, T. Gong, A. Sharma, P. W. Burridge, B. Patlolla, A. S. Lee, H. Wu, R. E. Beygui, S. M. Wu, R. C. Robbins, D. M. Bers, J. C. Wu, Screening drug-induced arrhythmia [corrected] using human induced pluripotent stem cell-derived cardiomyocytes and low-impedance microelectrode arrays. *Circulation* **128**, S3–S13 (2013).

36. C. Funck-Brentano, Y. Kibleur, F. Le Coz, J. M. Poirier, A. Mallet, P. Jaillon, Rate dependence of sotalol-induced prolongation of ventricular repolarization during exercise in humans. *Circulation* **83**, 536–545 (1991).

37. J. R. Teerlink, R. Diaz, G. M. Felker, J. J. V. Mc Murray, M. Metra, S. D. Solomon, K. F. Adams, I. Anand, A. Arias-Mendoza, T. Biering-Sørensen, M. Böhm, D. Bonderman, J. G. F. Cleland, R. Corbalan, M. G. Crespo-Leiro, U. Dahlström, L. E. Echeverria, J. C. Fang, G. Filippatos, C. Fonseca, E. Goncalvesova, A. R. Goudev, J. G. Howlett, D. E. Lanfear, J. Li, M. Lund, P. Macdonald, V. Mareev, S.-I. Momomura, E. O'Meara, A. Parkhomenko, P. Ponikowski, F. J. A. Ramires, P. Serpytis, K. Sliwa, J. Spinar, T. M. Suter, J. Tomcsanyi, H. Vandekerckhove, D. Vinereanu, A. A. Voors, M. B. Yilmaz, F. Zannad, L. Sharpsten, J. C. Legg, C. Varin, N. Honarpour, S. A. Abbasi, F. I. Malik, C. E. Kurtz; GALACTIC-HF Investigators, Cardiac myosin activation with omecamtiv mecarbil in systolic heart failure. *N. Engl. J. Med.* **384**, 105–116 (2021).

38. F. I. Malik, J. J. Hartman, K. A. Elias, B. P. Morgan, H. Rodriguez, K. Brejc, R. L. Anderson, S. H. Sueoka, K. H. Lee, J. T. Finer, R. Sakowicz, R. Baliga, D. R. Cox, M. Garard, G. Godinez, R. Kawas, E. Kraynack, D. Lenzi, P. P. Lu, A. Muci, C. Niu, X. Qian, D. W. Pierce, M. Pokrovskii, I. Suehiro, S. Sylvester, T. Tochimoto, C. Valdez, W. Wang, T. Katori, D. A. Kass, Y.-T. Shen, S. F. Vatner, D. J. Morgans, Cardiac myosin activation: A potential therapeutic approach for systolic heart failure. *Science* **331**, 1439–1443 (2011).

39. V. J. Planelles-Herrero, J. J. Hartman, J. Robert-Paganin, F. I. Malik, A. Houdusse, Mechanistic and structural basis for activation of cardiac myosin force production by omecamtiv mecarbil. *Nat. Commun.* **8**, 190 (2017).

40. Y. T. Shen, F. I. Malik, X. Zhao, C. Depre, S. K. Dhar, P. Abarzua, D. J. Morgans, S. F. Vatner, Improvement of cardiac function by a cardiac Myosin activator in conscious dogs with systolic heart failure. *Circ. Heart Fail.* **3**, 522–527 (2010).

41. F. Morady, A. Kadish, M. de Buitleir, W. H. Kou, H. Calkins, S. Schmaltz, S. Rosenheck, J. Sousa, Prospective comparison of a conventional and an accelerated protocol for programmed ventricular stimulation in patients with coronary artery disease. *Circulation* **83**, 764–773 (1991).

42. H. Zhao, Y. Kim, H. Wang, X. Ning, C. Xu, J. Suh, M. Han, G. J. Pagan-Diaz, W. Lu, H. Li, W. Bai, O. Aydin, Y. Park, J. Wang, Y. Yao, Y. He, M. T. A. Saif, Y. Huang, R. Bashir, J. A. Rogers, Compliant 3D frameworks instrumented with strain sensors for characterization of millimeter-scale engineered muscle tissues. *Proc. Natl. Acad. Sci. U.S.A.* **118**, e2100077118 (2021).

43. G. R. Mines, On dynamic equilibrium in the heart. *J. Physiol.* **46**, 349–383 (1913).

44. W. E. Garrey, The nature of fibrillary contraction of the heart.—Its relation to tissue mass and form. *Am. J. Physiol.* **33**, 397–414 (1914).

45. T. Lewis, *The mechanism and graphic registration of the heart beat* (Shaw, 1920).

46. M. Synofzik, W. M. C. van Roon-Mom, G. Marckmann, H. A. van Duyvenvoorde, H. Graessner, R. Schule, A. Aartsma-Rus, Preparing n-of-1 antisense oligonucleotide treatments for rare neurological diseases in Europe: Genetic, regulatory, and ethical perspectives. *Nucleic Acid Ther.* **32**, 83–94 (2022).

47. K. K. Aras, N. R. Faye, B. Cathey, I. R. Efimov, Critical volume of human myocardium necessary to maintain ventricular fibrillation. *Circ. Arrhythm. Electrophysiol.* **11**, e006692 (2018).

48. A. M. Gacita, D. E. Fullenkamp, J. Ohiri, T. Pottinger, M. J. Puckelwartz, M. A. Nobrega, E. M. McNally, Genetic variation in enhancers modifies cardiomyopathy gene expression and progression. *Circulation* **143**, 1302–1316 (2021).

49. D. E. Fullenkamp, A. B. Willis, J. L. Curtin, A. P. Amaral, K. T. Dittloff, S. I. Harris, I. A. Chychula, C. W. Holgren, P. W. Burridge, B. Russell, A. R. Demonbreun, E. M. M. Nally, Physiological stress improves stem cell modeling of dystrophic cardiomyopathy. *Dis. Model. Mech.* **17**, dmm050487 (2024).

50. P. W. Burridge, E. Matsa, P. Shukla, Z. C. Lin, J. M. Churko, A. D. Ebert, F. Lan, S. Diecke, B. Huber, N. M. Mordwinkin, J. R. Plews, O. J. Abilez, B. Cui, J. D. Gold, J. C. Wu, Chemically defined generation of human cardiomyocytes. *Nat. Methods* **11**, 855–860 (2014).

51. D. F. Selgrade, D. E. Fullenkamp, I. A. Chychula, B. Li, L. Dellefave-Castillo, A. D. Dubash, J. Ohiri, T. O. Monroe, G. Tomar, C. Holgren, P. W. Burridge, A. L. George Jr., A. R. Demonbreun, M. J. Puckelwartz, S. A. George, I. R. Efimov, K. J. Green, E. M. M. Nally,

Susceptibility to innate immune activation in genetically-mediated myocarditis. *J. Clin. Invest.* **134**, e180254 (2024).

52. J. T. Kim, W. Ouyang, H. Hwang, H. Jeong, S. Kang, S. Bose, S. S. Kwak, X. Ni, H. Kim, J. Park, H. Chen, A. Soetikno, J. Kim, S. Xu, L. P. Chamorro, J. A. Rogers, Dynamics of plosive consonants via imaging, computations, and soft electronics. *Proc. Natl. Acad. Sci. U.S.A.* **119**, e2214164119 (2022).

53. R. M. Geiger, M. G. Klein, N. Fatima, R. E. Goldstein, M. J. Krantz, M. C. Haigney, T. P. Flagg, Rapid assessment of proarrhythmic potential using human iPSC-derived cardiomyocytes. *JACC Clin. Electrophysiol.* **6**, 1860–1862 (2020).

54. Q. Wu, P. Zhang, G. O'Leary, Y. Zhao, Y. Xu, N. Rafatian, S. Okhovatian, S. Landau, T. A. Valiante, J. Travas-Sejdic, M. Radisic, Flexible 3D printed microwires and 3D microelectrodes for heart-on-a-chip engineering. *Biofabrication* **15**, 035023 (2023).

55. B. Gu, X. Li, C. Yao, X. Qu, M. Mao, D. Li, J. He, Integration of microelectrodes and highly-aligned cardiac constructs for in situ electrophysiological recording. *Microchem. J.* **190**, 108587 (2023).

56. M. Rieger, C. Dellenbach, J. Vom Berg, J. Beil-Wagner, A. Maguy, S. Rohr, Enabling comprehensive optogenetic studies of mouse hearts by simultaneous opto-electrical panoramic mapping and stimulation. *Nat. Commun.* **12**, 5804 (2021).

57. S. S. Nunes, J. W. Miklas, J. Liu, R. Aschar-Sobbi, Y. Xiao, B. Zhang, J. Jiang, S. Massé, M. Gagliardi, A. Hsieh, N. Thavandiran, M. A. Laflamme, K. Nanthakumar, G. J. Gross, P. H. Backx, G. Keller, M. Radisic, Biowire: A platform for maturation of human pluripotent stem cell–derived cardiomyocytes. *Nat. Methods* **10**, 781–787 (2013).